3-26-2020

Microstructure-based numerical simulation of themechanical properties and fracture of a Ti-Al3Ti core-shell structured particulate reinforced A356 composite

Siming Ma

Xuezheng Zhang

Tijun Chen

Xiaoming Wang

Materials and Design 191 (2020) 108685

Contents lists available at ScienceDirect

Materials and Design

journal homepage: www.elsevier.com/locate/matdes

Microstructure-based numerical simulation of the mechanical properties and fracture of a Ti-Al_3Ti core-shell structured particulate reinforced A356 composite

Siming Ma [a], Xuezheng Zhang [b], Tijun Chen [b,*], Xiaoming Wang [a,*]

[a] School of Engineering Technology, Purdue University, 401 N. Grant Street, West Lafayette, IN 47906, USA
[b] State Key Laboratory of Advanced Processing and Recycling of Nonferrous Metals, Lanzhou University of Technology, Lanzhou 730050, PR China

HIGHLIGHTS

- Tensile and fracture of a Ti-Al_3Ti core-shell structured particulate reinforced A356 composite were studied
- Constitutive behaviors of the CS particulates are obtained by a reverse analysis algorithm from nano-indentation results
- The high ductility of the Ti-Al_3Ti CS particulate reinforced A356 composite is is well explained by simulation
- The predicted fracture behavior shows a satisfactory agreement with the observation in in-situ tensile test

GRAPHICAL ABSTRACT

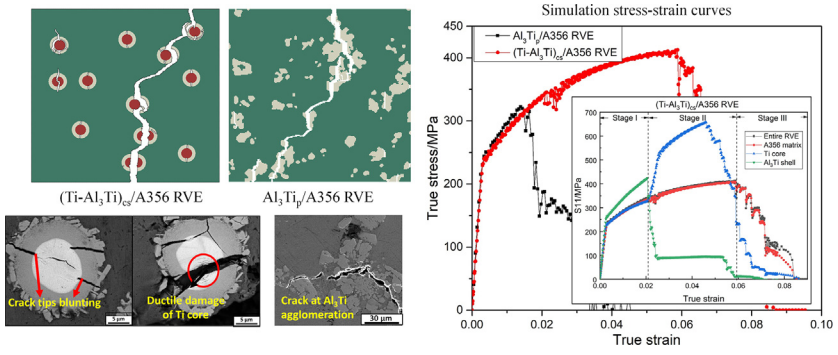

ARTICLE INFO

Article history:
Received 20 February 2020
Received in revised form 22 March 2020
Accepted 25 March 2020
Available online 26 March 2020

Keywords:
Aluminum matrix composite
Metal matrix composite
Core–shell structure
Finite element analysis
Mechanical property
Representative volume element

ABSTRACT

A microstructure-based numerical simulation is performed to understand the mechanical properties and fracture of a Ti-Al_3Ti core-shell structured particulate reinforced A356 composite ($(Ti\text{-}Al_3Ti)_{cs}$/A356). A series of two-dimensional (2D) representative volume element (RVE) models are generated automatically by embedding Ti-Al_3Ti core-shell structured particulates in an A356 matrix. Microstructure-based 2D RVE of monolithic Al_3Ti particulate reinforced A356 composite (Al_3Ti_p/A356) is also simulated for comparison. The ductile fracture of both Ti core and A356 matrix as well as the brittle fracture of the Al_3Ti shell are considered. The simulation confirms that the high elongation of the $(Ti\text{-}Al_3Ti)_{cs}$/A356 composite is attributed to the uniform distribution of the overall ductile globular reinforcing particulates, which prevent a premature failure effectively by reducing local stress concentration both on and inside the core-shell structured particulates. The surrounding ductile phases of the Al_3Ti shell blunt the crack tips effectively and, therefore, restricting the propagation of the cracks in a nominal strain range of 2.2%–6.1%. For both $(Ti\text{-}Al_3Ti)_{cs}$/A356 and Al_3Ti_p/A356 composites, the simulation results are in good agreement with microstructural observations during an in-situ tensile test in a scanning electron microscope.

* Corresponding authors.
E-mail addresses: ma512@purdue.edu (S. Ma), chentj@lut.cn (T. Chen), wang1747@purdue.edu (X. Wang).

https://doi.org/10.1016/j.matdes.2020.108685

1. Introduction

Al-Si casting alloys are widely used by the automobile and aerospace industries for their good mechanical properties, castability and corrosion resistance etc. [1–3]. To further enhance the mechanical properties of Al-Si alloys, one effective way is to fabricate composites with the addition of in-situ ceramic reinforcing particulates [4–7]. Amongst various candidate reinforcements, Al_3Ti particulate has high modulus, light weight and strong bonding with the Al-Si alloy matrix [8,9]. In-situ Al_3Ti particulate reinforced A356 composites have shown evident strength improvement in other research. However, in spite of the increased strength, the ductility of Al_3Ti_p/A356 composites is affected adversely due to the high brittleness, coarse particle size, irregular morphology and agglomeration of the reinforcing particulates [10–13].

In order to increase the ductility while maintaining the high strength of aluminum matrix composites, core-shell structured reinforcing particulates are produced in-situ by adding metallic particles to react with the matrix alloy during processing. The core-shell structured reinforcing particulate typically consists of a ductile metallic core and a layer of intermetallic shell [14]. For the core-shell structured particulate reinforced metal matrix composites, micro cracks initiate in the brittle intermetallic shells. However, the propagation of the cracks is arrested by the reinforcement/matrix and reinforcement/core interfaces where the crack tips are blunted by the ductile Al matrix outside and the metallic core inside [15]. Different kinds of core-shell structured particulates, such as Fe–Al_xFe_y, Ni-Al_xNi_y, Ti-Al_3Ti, were reported to reinforce Al alloys while showing improved either compressive or tensile ductility [16–18]. Amongst these studies, an A356 matrix composite reinforced with Ti-Al_3Ti core-shell particulates ($(Ti\text{-}Al_3Ti)_{cs}$) showed an improved tensile elongation while maintaining its high strength compared to a monolithic Al_3Ti particulate reinforced A356 composite [15]. The high ductility of the $(Ti\text{-}Al_3Ti)_{cs}$/A356 composites is attributed to the uniform distribution of globular core-shell structured particulates, which eliminates particulate agglomeration and irregular shape particulates. Another attribution is the compact microstructure from powder thixoforming, which fills up voids with liquid [19]. However, a detailed study on the deformation and fracture behaviors of these core-shell particulate reinforced composites is still limited to a microscopic scale, i.e., on the formation and propagation of cracks in relationship to the constitutive phases of the composites.

Recently, microstructure-based numerical simulations have been widely employed to predict macroscopic mechanical properties of multiphase materials. Amongst different methods, representative volume element (RVE) models take constitutive properties and microstructural features (volume fraction, size, shape, and distribution) to represent macroscopic properties [20]. A microstructure-based RVE simulation has been applied to predict the flow behaviors, damage evolution, and fracture of a variety of multiphase materials, such as dual-phase steels [21–23] and metal matrix composites [24–27]. The method is also promising in simulating damage evolution at a microscopic level and is helpful in understanding and predicting the enhanced ductility of the $(Ti\text{-}Al_3Ti)_{cs}$/A356 composites.

The present study intends to investigate the mechanical properties and fracture behaviors of a $(Ti\text{-}Al_3Ti)_{cs}$/A356 composite via a microstructure-based numerical simulation method. A series of two-dimensional (2D) RVEs are generated as representatives of the (Ti-

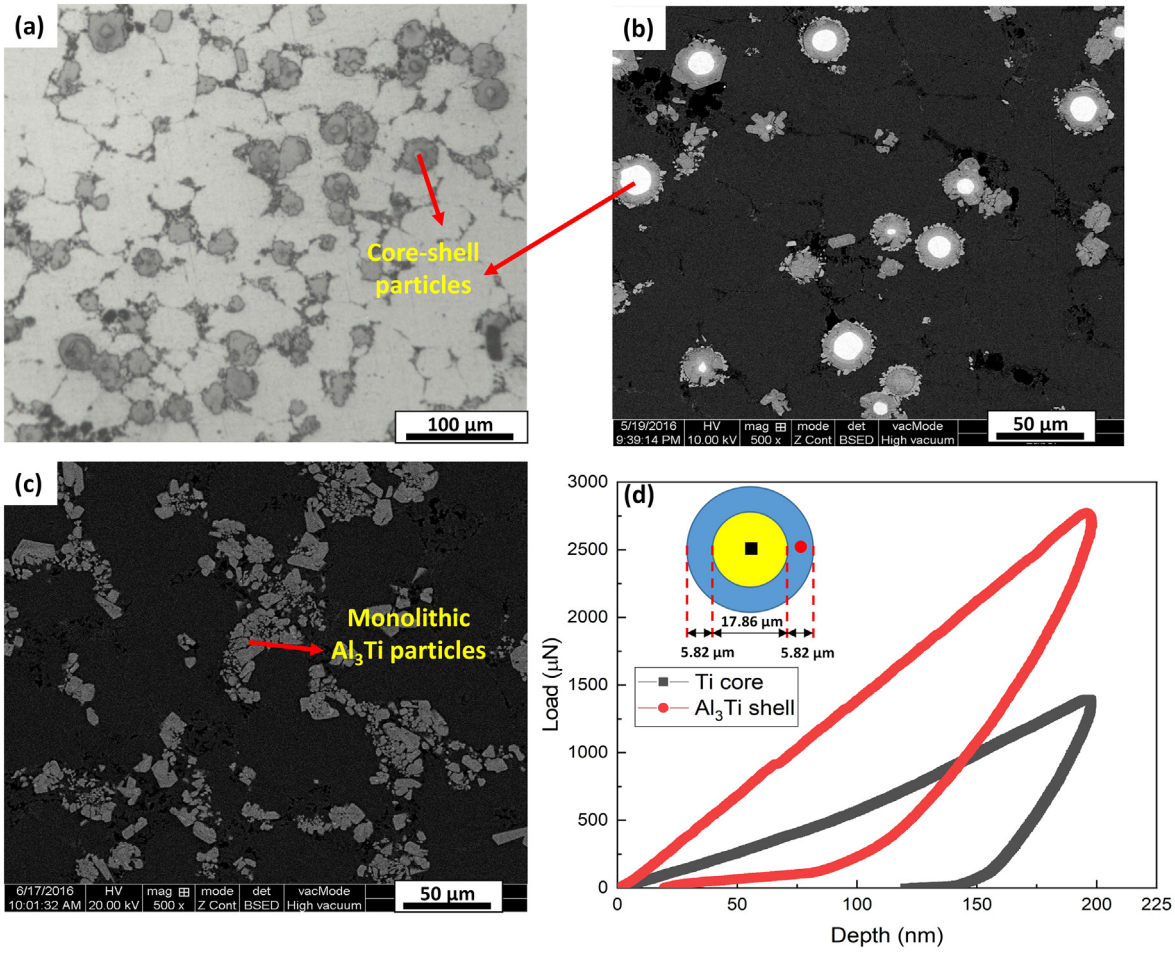

Fig. 1. (a) OM and (b) BSE images of $(Ti\text{-}Al_3Ti)_{cs}$/A356 composite; (c) BSE image of Al_3Ti_p/A356 composite; (d) nano-indentation depth-load curves of Ti core and Al_3Ti shell (inserted schematic image shows the average core diameter and shell thickness of the core-shell particulates).

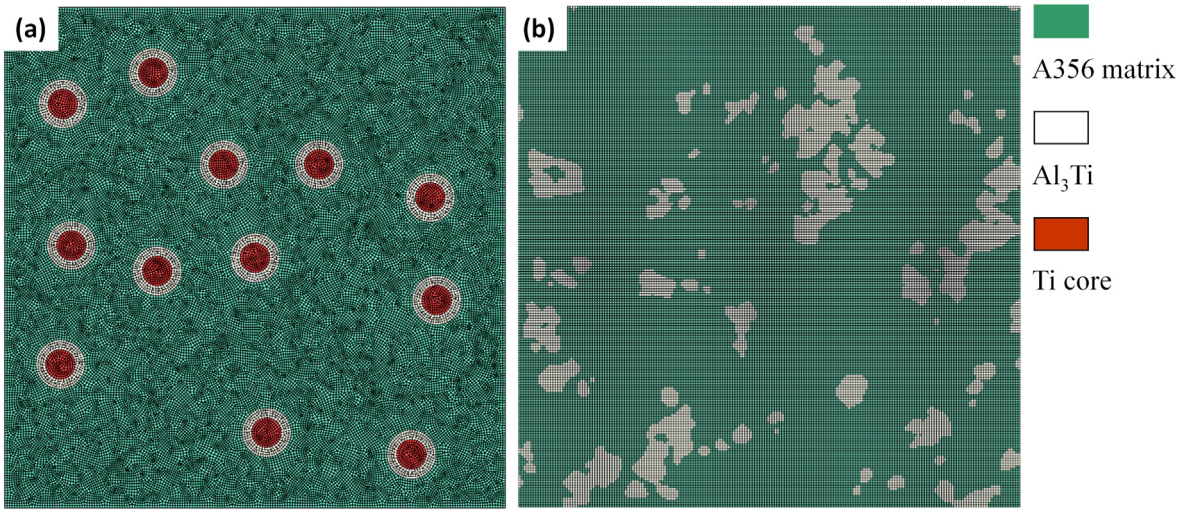

Fig. 2. 2D RVE example models and corresponding constitutive phases of (a) the $(Ti\text{-}Al_3Ti)_{cs}$/A356 composite model; (b) the Al_3Ti_p/A356 composite.

$Al_3Ti)_{cs}$/A356 composite and submitted for finite element (FE) simulation under uniaxial tensile loading, with the consideration of the damage of constitutive phases. In addition, the microstructure-based simulation is also conducted on the 2D RVEs of a monolithic Al_3Ti_p/A356 composite for comparison, in order to elucidate the mechanisms of the improved ductility of the $(Ti\text{-}Al_3Ti)_{cs}$/A356 composite. Furthermore, the damage evolution and fracture behavior of the two composites predicted by simulation are compared to experimental findings during in-situ tensile test under a scanning electron microscope (SEM).

2. Materials and experiment

A powder thixoforming process was employed to synthesize the $(Ti\text{-}Al_3Ti)_{cs}$ particulates in an A356 alloy matrix. The A356 alloy matrix was made from gas atomized powders of pure Al and a hypereutectic Al-Si alloy to a final composition of (in wt%) of Si 7.51, Mg 0.22, Fe 0.12, Ti 0.10 and balanced Al. Purity Ti powders (99.99% Ti) were added to react with the alloy matrix and to form the reinforcing particulates during the thixoforming process. Pure Ti powder, A356 alloy matrix and pure Al powder were mixed with weight percentage of 4.57, 87.71 and 7.72, respectively, for a target 10% volume fraction of monolithic Al_3Ti particulates after a complete reaction. The addition of pure Al powder is to compensate the cost of Al as Ti converted to Al_3Ti. The powders were blended thoroughly in a planetary ball-milling machine with the rotation speed, ball-to-powder weight ratio and mixing time being 100 rpm, 5:1 and 30 min, respectively. The powder mixture was then cold-compressed into green billets (Φ45 mm × 16 mm) by a hydraulic compression machine. The green billets were subsequently heated up to 600 °C (a semisolid temperature for the A356 matrix alloy) and kept for 50 min to synthesize the $Ti\text{-}Al_3Ti$ core-shell reinforcements in a tubular vacuum furnace (vacuum < 10^{-2} Torr). For comparison, some green billets had been kept for another 180 min under identical condition for a complete reaction to produce a monolithic Al_3Ti phase in the particulates. All the heated billets were placed in a die with a cavity size of Φ55 mm × 60 mm and thixoforged under 150 MPa. Moreover, the A356 matrix alloy without the addition of Ti powders was also cold compacted, heated and thixoformed under identical processing conditions as the reference material.

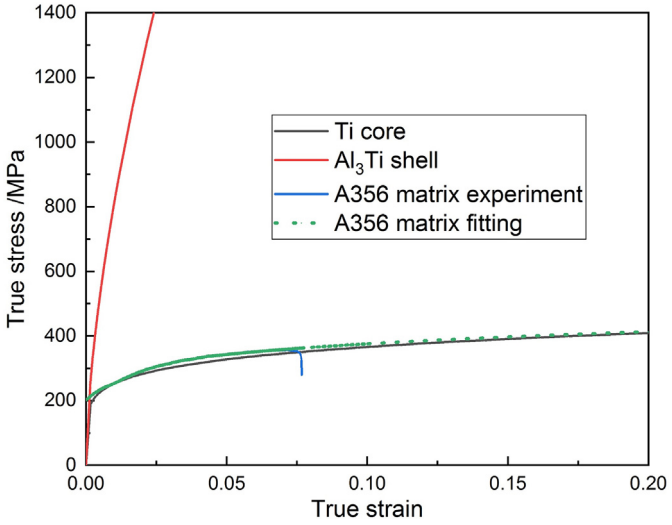

Fig. 3. Strain-stress relationships of Ti core and Al_3Ti shell calculated by the reverse analysis algorithms and A356 matrix by extrapolating from the experimental curve.

The typical microstructures of $(Ti\text{-}Al_3Ti)_{cs}$/A356 and Al_3Ti_p/A356 composites are shown in Fig. 1(a)–(c), which were taken from the centers of the thixoformed products by a MEF-3 optical microscope (OM) and a Quanta FEG 450 SEM. For the $(Ti\text{-}Al_3Ti)_{cs}$/A356 composite, $Ti\text{-}Al_3Ti$ core-shell particulates are generally globular and well dispersed in the A356 matrix. The diameters of Ti core, shell thickness and volume fraction of the $(Ti\text{-}Al_3Ti)_{cs}$ particulates were analyzed from the SEM images by *Image-Pro Plus 6.0* software. The average Ti core diameter, the average Al_3Ti shell thickness and the volume fraction of the $(Ti\text{-}Al_3Ti)_{cs}$ particulates are 17.86 μm, 5.82 μm and 8.8%, respectively, as shown in the inserted schematic drawing in Fig. 1(d). In comparison, in the Al_3Ti_p/A356 composite, only monolithic blocky Al_3Ti phase particulates are observed, agglomerating as large-sized clusters (>50 μm) with an irregular outline, as shown in Fig. 1(c).

Tensile tests were conducted on a WDW-100D universal material testing machine at a strain rate of 0.5 mm min^{-1}. Tensile specimens were machined from the center region of each thixoformed product with a rectangular cross-section of 2.5 mm by 1.5 mm. The gauge length was 10 mm. The fracture strain (ε_f) was determined by $\varepsilon_f = \ln(A_0 / A_f)$ for each material, where A_0 is the initial cross section area and A_f is the cross section area at fracture. Additionally, in order to track the crack path, in-situ tensile tests were performed in a Quanta FEG 450 SEM with single edge notched rectangular specimens. The specimen has a

Table 1
Inputting parameters for the reverse solution algorithm.

Phase	υ	C/GPa	h_r/h_m	p_{ave}/GPa	P_m/mN
Ti core	0.3 [33]	28.3	0.633	1.33	1.396
Al_3Ti	0.25 [34]	112	0.409	3.41	2.772

Table 2
Parameters solved by the reverse solution algorithm.

	E^*/GPa	$\sigma_{0.033}$/MPa	E/GPa	n	σ_y/MPa
Ti core	116.1	309	119.4	0.161	188
Al_3Ti	153.0	1750	169.1	0.624	245

thickness of 1 mm, a width of 3.5 mm and the gauge length of 4 mm. A 30° V-shape notch is set on one edge of the sample with the notch depth of 1 mm. The samples were tensioned utilizing a Kammrath-Weiss micro-tensile stage with a strain rate of $2 \times 10^{-4}\ s^{-1}$, during which it was stopped repeatedly for scanning the crack by SEM. The depth-load curves of the $(Ti\text{-}Al_3Ti)_{cs}$/A356 composite are used to obtain the constitutive properties by a reverse analysis method. The tests were conducted on a MTS Nano Indenter XP system with a typical diamond Berkovich tip.

3. Microstructure-based finite element (FE) simulation

3.1. RVE generation

To simulate the $(Ti\text{-}Al_3Ti)_{cs}$/A356 composite, a series of two-dimensional (2D) RVEs were automatically generated. Fig. 2(a) is an RVE example showing spherical Ti-Al_3Ti core-shell structured particulates distributed randomly in an A356 matrix, with a volume fraction of 8.8%. The thickness of the Al_3Ti shell and the diameter of the Ti core were set as 5.82 μm and 17.86 μm, respectively, based on the results of image analysis.

To understand the size effects of the RVE simulation on the composites, a cell model (with one particulate in the center of RVE), and 200 μm, 300 μm, and 500 μm edge-sized RVEs (with 5, 12, and 32 randomly distributed particulates, respectively) were selected. The simulation results begin to converge when the RVE size exceeds 200 μm, as indicated in Fig. 5 later on. Considering the number of particulates in a RVE as well as the computation cost in FE simulation, the RVE size is set as 300 μm in the following simulation unless specifically noted. Additionally, a group of ten different RVE models was generated with a random distribution of particulates for comparison to study the effects of particle distribution.

The microstructure-based RVE models of the Al_3Ti_p/A356 composite were generated by the binarization of backscattered electron (BSE) images. An example is presented in Fig. 2(b). Five different RVE models were simulated with the same RVE size of 300 μm for the $(Ti\text{-}Al_3Ti)_{cs}$/A356 composite. For all the RVE models mentioned above, the interface nodes were assumed to be strictly bonded, by considering the strong interfacial bonding between Al_3Ti and the matrix Al and Al_3Ti and the Ti cores [8,17,28,29]. A global mesh seed size of 1.5 μm was applied on the RVEs of the two composites, as shown in Fig. 2. The element number in each RVE model was approximately 40,000.

3.2. Constitutive behavior

The A356 alloy matrix is treated as a homogenous and isotropic elasto-plastic material. The Young's Modulus is set as 69 GPa and Poisson ratio is 0.33 [30]. The stress-strain curve of A356 alloy is extrapolated from the experimental uniaxial tensile stress-strain curve of A356 alloy matrix, as shown in Fig. 3. When the true strain is lower than 7.2% (approximately the necking point), the experimental stress-strain relation is maintained. With a larger strain, extrapolation is employed with a power-law function of Eq. (1). The fitting parameters are $K = 518.12$ MPa and $n = 0.1425$.

$$\sigma = K\varepsilon_p^n \tag{1}$$

The elastic and plastic properties of the Ti core and Al_3Ti in both the shells and the monolithic Al_3Ti particulates are obtained from their nano-indentation force-displacement curves with a reverse analysis algorithm as proposed in Dao's work [31]. The Al_3Ti phase in both Al_3Ti_p/A356 and $(Ti\text{-}Al_3Ti)_{cs}$/A356 composites having identical properties is assumed in this study for simplicity.

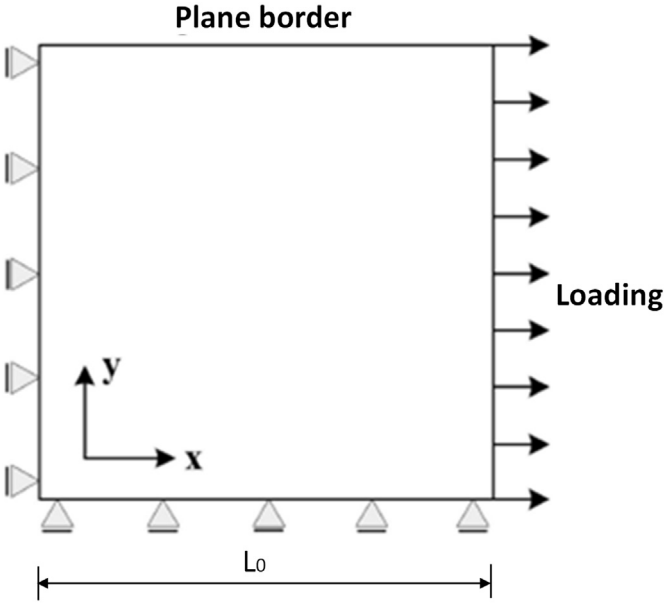

Fig. 4. Schematic illustration of boundaries conditions and loading on RVE models.

The reverse analysis algorithm of Dao's work assumes that the plastic behavior of pure metals and alloys could be closely approximated by a power law description as Eq. (2):

$$\sigma = \sigma_y\left(1 + \frac{E}{\sigma_y}\varepsilon_p\right)^n \tag{2}$$

where σ_y is the yield stress, ε_p is true plastic strain, n is the strain hardening exponent. E is the Young's modulus.

The typical load-depth (P-h) response of an elastic-plastic material to sharp indentation generally follows Kick's law (Eq. (3)),

$$P = Ch^2 \tag{3}$$

where C is the loading curvature, which is obtained by fitting the loading-depth curves in Fig. 1(d).

The hardness p_{ave} is defined as the average contact pressure, expressed as Eq. (4).

$$p_{ave} = \frac{P_m}{A_m} \tag{4}$$

where A_m is the true projected contact area corresponding to the maximum load P_m.

The reduced Young's modulus E^* is defined as:

$$E^* = \left[\frac{1-\upsilon^2}{E} + \frac{1-\upsilon_i^2}{E_i}\right] \tag{5}$$

where E_i is Young's modulus of the indenter and υ_i is its Poisson's ratio. For a diamond indenter, $E_i = 1000$ GPa, $\upsilon_i = 0.07$. E and υ is the young's modulus and Poisson's ratio of the tested material, respectively [32]. From the loading-depth curves in Fig. 1(d), the initial input parameters C, h_r/h_m (the ratio of residual indentation depth h_r to the maximum indentation depth h_m), p_{ave} (hardness), P_m (maximum load) are obtained, as shown in Table 1.

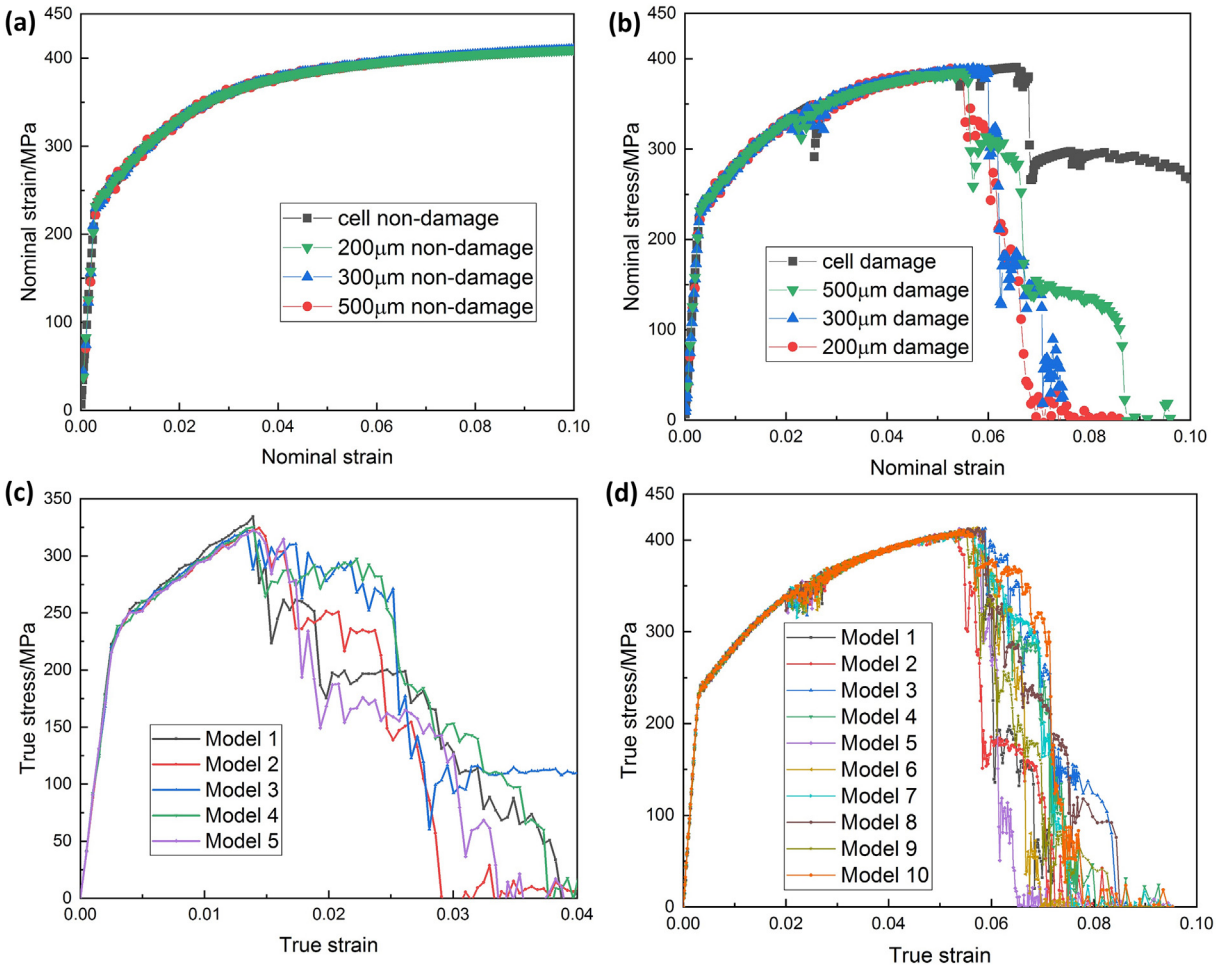

Fig. 5. Simulated stress-strain curves of (a) $(Ti\text{-}Al_3Ti)_{cs}$/A356 non-damaged RVEs and (b) $(Ti\text{-}Al_3Ti)_{cs}$/A356 damaged RVEs with different size; (c) five different Al_3Ti_p/A356 RVE models (RVE size = 300 μm) and (d) ten different $(Ti\text{-}Al_3Ti)_{cs}$/A356 RVE models.

The dimensionless functions (π-functions) in the present work are listed as Eqs. (6) to (9):

$$C = \sigma_{0.033}\Pi_1\left(\frac{E^*}{\sigma_{0.033}}\right) \tag{6}$$

$$\frac{1}{E^* h_m}\frac{dP}{dh_{h_m}} = \Pi_2\left(\frac{E^*}{\sigma_{0.033}}, n\right) \tag{7}$$

$$\frac{p_{ave}}{E^*} = \Pi_4\left(\frac{h_r}{h_m}\right) \tag{8}$$

$$\Pi_6 = \frac{1}{E^*\sqrt{A_m}}\frac{dP}{dh_{h_m}} = c^* \tag{9}$$

Detailed parameters in each π-function are given in the appendix of Dao's work [31]. For the Berkovich indenter, c^* is 1.2370 [35].

Inputting the parameters in Table 1, the solved parameters for each phase are listed in Table 2. E^* and A_m are calculated by Eqs. (8) and (9). $\sigma_{0.033}$ and n can be solved by Eqs. (6) and (7), respectively. The young's moduli E of Al_3Ti and the Ti core are solved by Eq. (5) after obtaining E^*. The values of solved young's moduli are close to the experimental data of other work [36] (E_{Ti} = 115GPa) and [34] (E_{Al3Ti} = 170 MPa). The yield stress σ_y can then be solved by Eq. (10).

$$\sigma_{0.033} = \sigma_y\left(1 + \frac{E}{\sigma_y}0.033\right)^n \tag{10}$$

Therefore, the stress-strain relationships of the Ti-core and the Al_3Ti phase can be calculated by using Hooke's law ($\sigma = E\varepsilon$) and Eq. (2) with the parameters of E, n, and σ_y. Fig. 3 summarizes the stress-strain curves of the two phases as well as the extrapolated stress-strain curve of the A356 alloy matrix.

3.3. Damage mechanisms

The following damage mechanisms are involved in the present simulation: the ductile failure of the A356 matrix and the Ti cores as well as the brittle fracture of the Al_3Ti phase. To describe the ductile damage of the A356 matrix and Ti core, a damage parameter D_η, as Eq. (11), defined by Rice and Tracey [37] is adopted.

$$D_\eta = \int_0^{\varepsilon_p} e^{\eta} d\varepsilon_p \tag{11}$$

where $\eta = \sigma_m/\sigma_y$ is the stress triaxiality. σ_m is the hydrostatic stress, σ_y is the von Mises stress and ε_p is cumulative plastic strain.

Ductile failure occurs when the local damage parameter D_η exceeds a critical value $D_{\eta c}$. To determine $D_{\eta c}$ for the ductile phases, a single element uniaxial tensile simulation was carried out in Qing's work [38]. In

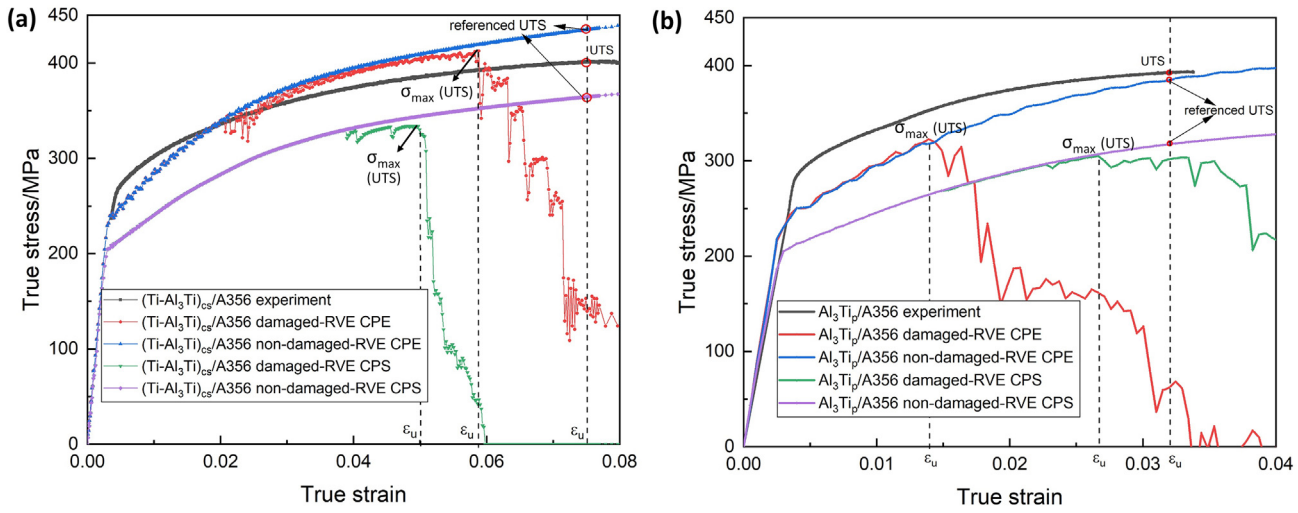

Fig. 6. Comparison of experimental and simulated true stress-strain curves with different element type (a) $(Ti\text{-}Al_3Ti)_{cs}$/A356; (b) Al_3Ti_p/A356.

the present work, the true fracture strain (ε_f) is 0.3 for A356 matrix. For Ti, ε_f is set as 0.5, according to the experimental work of Srinivasan et al. [39]. Single plane strain element of A356 matrix or Ti is given by the stress-strain relationships in Fig. 3 and is tensioned to its facture strain (ε_f). The D_η value of the element at the fracture strain is taken as $D_{\eta c}$, which is calculated as 0.54 and 0.825 for the A356 matrix and Ti core, respectively.

A maximum principal stress criterion is applied to determine the brittle failure of the Al_3Ti phase. The maximum strength and the strain to failure were suggested as 805 MPa and 0.97%, respectively, based on the stress-strain response of an Al_3Ti + 0.3% Al alloy [40]. From the calculated stress-strain curve of the Al_3Ti phase in Fig. 3, the strength is 798 MPa at a strain of 0.97%, which is very close to the finding in literature [40]. Therefore, the critical principal stress is set as 798 MPa in the current work.

The microstructural damage and crack growth in the RVE models are modelled by an element removal approach. An Abaqus/Explicit Subroutine VUSDFLD is developed to realize the failure criterions above. The element of any constitutive phase (A356 matrix, Al_3Ti and Ti) is deleted once it met the fracture criterion of the corresponding phase. Besides, comparative simulations are conducted without applying the fracture criterions on RVE models. For simplicity, the RVE models are noted as "damaged models" when the fracture criterions are applied. Otherwise, they are noted as "non-damaged models".

3.4. Boundary conditions, loading and element type

The simulation is conducted with the Abaqus/Explicit software. Symmetrical boundary condition (SBC) is exerted on the RVE models for uniaxial tension [41,42], as shown in Fig. 4. All nodes on the bottom edge can only move in the x direction, while all nodes on the left edge can only move in the y direction. The top and right edges of the RVEs remain plane borders during tension. Displacement is given to all the nodes on the right edge, with a maximum nominal tensile strain of 0.1. 2D plane strain elements (Element type "CPE") and plane stress elements (Element type "CPS") are both applied for comparison in the simulation, as employed in related work [43,44].

The stress–strain curves are the output after the uniaxial tensile simulation. The nominal tensile strain is defined as the ratio between the displacement (U_x) and the length of RVE along the corresponding direction (U_x/L_0), while the nominal stress is defined the ratio between the tensile force (F_x) and the length of RVE perpendicular to the tensile direction (F_x/L_0). The true stress–strain (σ-ε) curve for each RVE is obtained by converting the obtained nominal stress (S)-strain (e) curve using Eqs. (12) and (13):

$$\sigma = S(1+e) \tag{12}$$

$$\varepsilon = \ln(1+e) \tag{13}$$

4. Results and discussion

4.1. Effect of RVE size, particle arrangement

The simulated stress–strain curves of different-sized $(Ti\text{-}Al_3Ti)_{cs}$/A356 RVE models are shown in Fig. 5(a). For non-damaged RVE models, the stress-strain curves show no evident differences regardless of the RVE size. Comparatively, in damaged models, the stress-strain curves reach a maximum stress first and then drop down at a certain nominal strain. The drop of simulated curves is attributed to the deletion of elements inside the RVE. It's also seen that for RVE size of 200, 300 and 500 μm, the drop occurs at a similar strain. But for the cell model, the stress drops down at a larger strain comparatively, because the cell model neglects the interaction of particles during the deformation. Therefore, a delayed fracture is expected.

Table 3
Prediction of ε_u, UTS, and elongation (El.) by 2D RVE models with comparison of experimental results.

		Experiment	2D non-damaged RVE[a]		2D damaged RVE	
			Plane strain element	Plane stress element	Plane strain element	Plane stress element
$(Ti\text{-}Al_3Ti)_{cs}$/A356	ε_u	7.5%	–	–	5.9% (0.7%)	4.8% (0.3%)
	UTS/MPa	373	401.83 (0.05)	337.22 (0.09)	387.65 (1.44)	315.63 (3.04)
	El.	8.3%	–	–	7.9% (0.5%)	6.0% (0.6%)
Al_3Ti_p/A356	ε_u	3.2%	–	–	1.5% (0.2%)	3.4% (0.3%)
	UTS/MPa	381	386.79 (2.45)	318.45 (1.17)	321.01 (5.12)	301.80 (1.76)
	El.	3.3%	–	–	3.6% (0.4%)	4.6% (0.7%)

[a] Data in the brackets refers to the standard deviation.

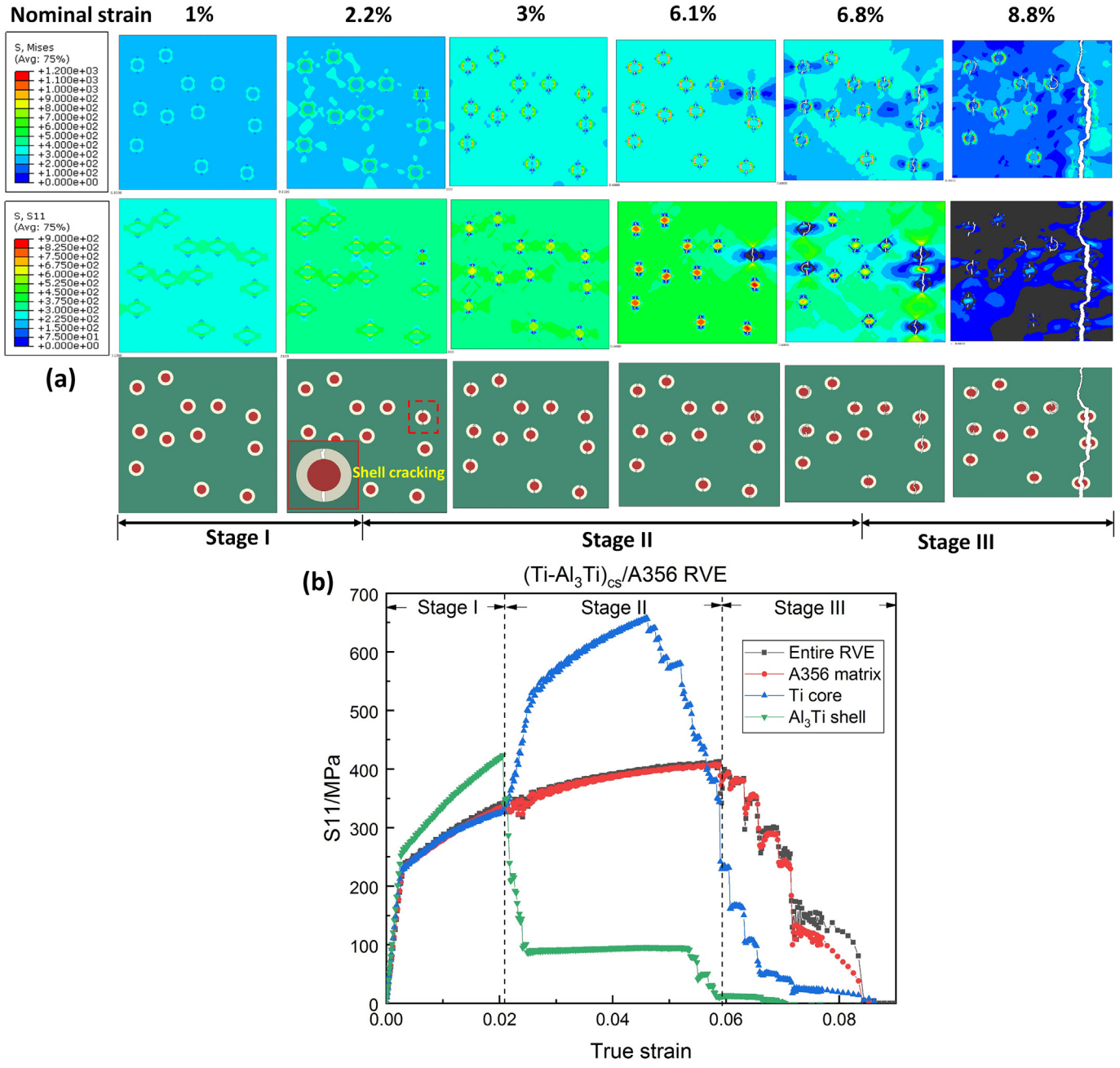

Fig. 7. (a) Mises stress, S11 stress tensor component distributions and damage evolution within $(Ti\text{-}Al_3Ti)_{cs}$/A356 RVE models during different deformation stages under tensile loading; (b) S11 stress partitions in constitutive phases under tensile loading in $(Ti\text{-}Al_3Ti)_{cs}$/A356 RVE.

From the simulated curves in Fig. 5(a) and (b), when the RVE size is 200 μm or larger, the stress-strain curves for both damaged and non-damaged RVEs show no evident differences. However, the 200 μm-sized RVE involves only five Ti-Al_3Ti particulates. Statistically, the inclusion number is too small for a RVE simulation [20]. For a 500 μm-sized RVE, the total element number is 120,000 approximately. The time for calculation increases significantly. Therefore, 300 μm is applied as the RVE size for all the RVE models in the following simulation.

Furthermore, from Fig. 5(c) and (d), it is clear that the simulated stress-strain curves of the models show little difference before the stress reaches the maximum, despite of the different arrangements of particulates between the models. However, when the stress-strain curves drop down, the stress-strain curves vary between the models. That is because the crack initiation and propagation are different in each model with a random arrangement of particulates.

4.2. Comparison of the experimental and simulation stress-strain curves

The true stress-strain curves of $(Ti\text{-}Al_3Ti)_{cs}$/A356 and Al_3Ti_p/A356 composites from simulation are compared with experimental results in Fig. 6(a) and (b), respectively. It is clear that the simulated curves have a lower yield stress than the experimental curves. The underestimation of the yield stress in a 2D RVE simulation has been pointed out in other work [45–47]. The reason is that the coefficients of thermal expansion (CTE) strengthening effect is not considered in the current work [48].

With the increase of strain, RVEs simulated with plane strain elements (CPE) show a work hardening rate compared to those simulated with plane stress elements (CPS). Consequently, the stress is overestimated with plane strain elements but is underestimated with plane stress elements, comparing with experimental curves. That is in

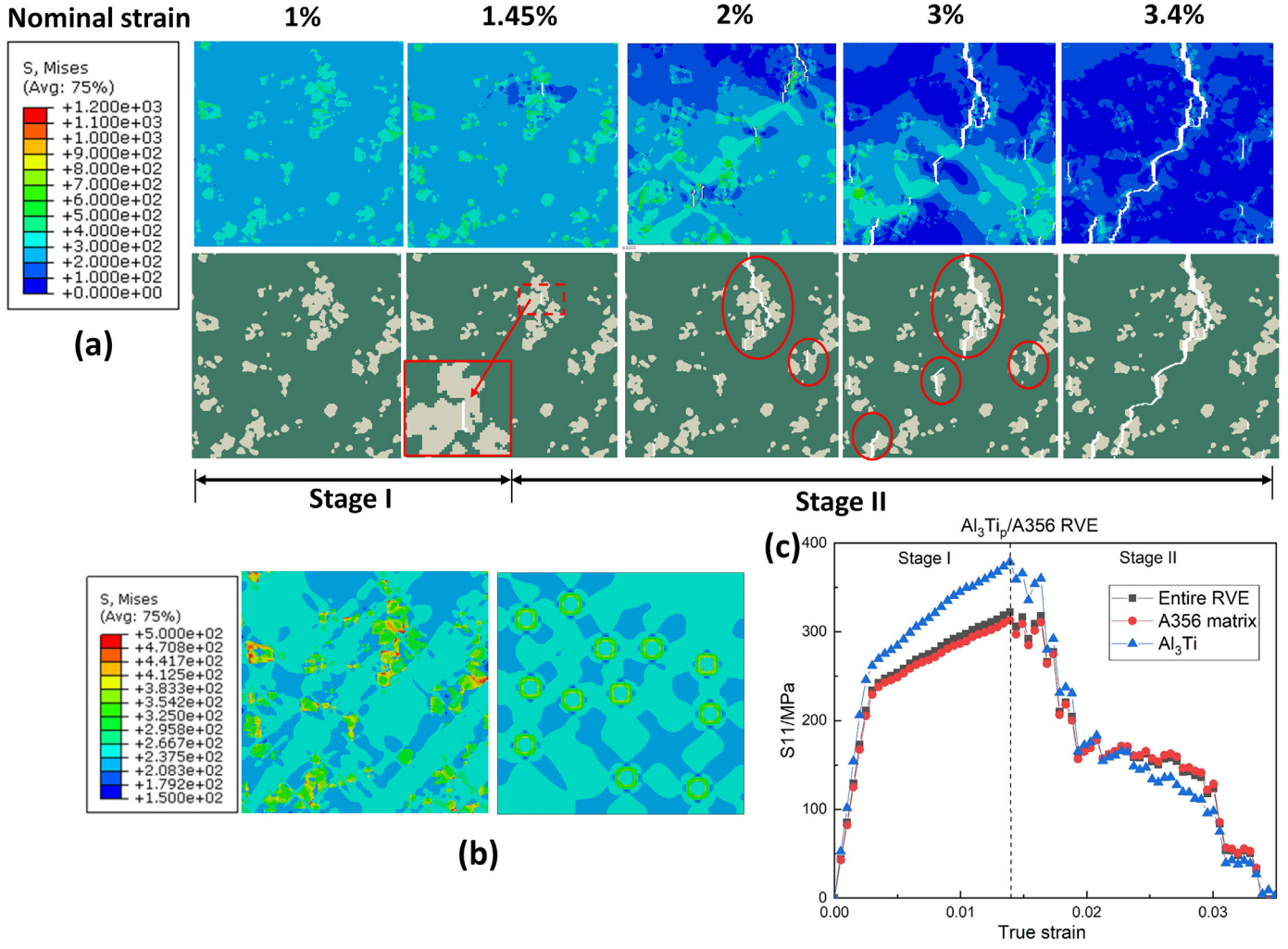

Fig. 8. (a) Mises stress, and damage evolution within Al_3Ti_p/A356 RVE models during different deformation stages under tensile loading; (b) stress concentration at Al_3Ti particulate agglomerations in the Al_3Ti_p/A356 RVE with comparison of the $(Ti\text{-}Al_3Ti)_{cs}$/A356 RVE at 1% nominal strain; (c) S11 stress partitions in constitutive phases under tensile loading in Al_3Ti_p/A356 RVE.

accordance with the 2D RVE simulation of dual-phase steels by Zhou et al. [43]. The difference between the simulated and experimental stress-strain curves is attributed to the discrepancy between the 2D and 3D stress states. The strain component exhibits an obvious variation along the thickness direction in Zhou's work. Therefore, the 2D plane strain assumption results in a discrepancy from the 3D situation. Simulation with plane stress elements (CPS), however, exhibits a global plastic instability at a very low strain. The stress is evidently smaller compared to the stress from experiment test in the 3D situation.

Furthermore, three parameters, ultimate tensile strength (UTS), the strain at UTS (ε_u), and elongation (El.), are extracted from experimental results and simulated stress-strain curves for comparison. For the experimental curves, according to the well-known Considere's criterion, plastic instability (necking point) occurs when the slope of the true stress–true strain curve [$d\sigma/d\varepsilon$] is equal to the true stress σ. This criterion is adopted to obtain the UTS and the corresponding strain (ε_u). The elongation (El.) is recorded as the largest engineering strain before the sample broken in tensile test.

For the simulated curves of non-damaged RVEs, the ultimate elongation is not considered. Therefore, the non-damaged models (simulated either by plane stress or plane strain element) having the same ε_u as the corresponding value from experimental tensile test is assumed. The stress at that ε_u is recorded as the "reference UTS" of these RVEs, in order to compare with the experimental UTS, as noted in Fig. 6 (a) and (b).

For a certain damaged RVE in this work, the UTS is defined as the maximum stress of the simulation curve, noted as σ_{max} in Fig. 6(b). The corresponding strain at σ_{max} is recorded as ε_u accordingly. The elongation (El.) is recorded as the strain when RVE model is totally torn apart. The UTS, ε_u and El. are averaged from the stress-strain curves of a group of RVE models. The results are presented in Table 3. The values in the bracket refer to the standard deviation.

In general, the simulated UTS values of RVEs with plane stress element are evidently lower than the experimental value, while RVEs with plane strain element give a better prediction. For the simulation of stress-strain curves with 2D RVE models, Paul [49] has reported similar findings when the sample thickness is 20% of its width. 2D RVE simulation with plane strain element gives a better prediction of the stress-strain curve comparing with the result of 3D RVE simulation. Additionally, from the research of Sun et al. [44], the plane stress element is more suitable in simulating thin tensile samples with their thickness is much smaller than the in-plane dimensions. Comparatively, the plane strain element is preferred for a tensile sample if its thickness comparative to its width. The tensile sample has a rectangular section of 2.5 mm × 1.5 mm in this study. Therefore, simulation with plane strain element should give a better estimation of the mechanical properties in 2D simulation, although it should still be noted that the 2D plane strain assumption is still a simplified approach compared to the 3D simulation.

Specifically, for the $(Ti\text{-}Al_3Ti)_{cs}$/A356 composite, when the damaged RVE models are applied with plane strain elements, the results show a

close prediction of the tensile strength, and ultimate elongation to the experimental data, as shown in Table 3. Comparatively, the damaged RVE models show an underestimation of uniform deformation strain attributed to the deletion of elements in presenting the damage behavior of the RVE models. The quick removal of failure elements after ε_u due to the rapid propagation of internal cracks results in evident losses in mass and stress inside RVEs, exaggerating the drop of stress on the simulated stress-strain curves compared to the experimental results. A similar exaggerated stress drop in 2D RVEs caused by element deletion was also presented in the simulation of dual phase (DP) steel [50].

4.3. Constitutive stress partition and damage evolution in RVE models

The details of the microscopic simulation, the distribution of stress field and the damage evolution, are presented in this section, employing the damaged RVE models with plane strain element. Additionally, the stress partition behavior of the constitutive phases (A356 matrix, Al_3Ti, and Ti core) is studied at different strains during the simulation. Because the loading is along the x direction, the S11 stress tensor component is obtained by averaging the S11 values from all the elements of the corresponding phase according to the first homogenization strategy [43].

4.3.1. $(Ti\text{-}Al_3Ti)_{cs}$/A356 composite

The Mises stress distribution, S11 distribution and damage evolution of a $(Ti\text{-}Al_3Ti)_{cs}$/A356 RVE model at different nominal tensile strains are shown in Fig. 7(a). The true stress-strain relationships of the constitutive phases are given for reference in Fig. 7(b). In general, the damage evolution in the $(Ti\text{-}Al_3Ti)_{cs}$/A356 composite follows a typical process of crack initiation, growth and linkage as reported [51].

The deformation process of $(Ti\text{-}Al_3Ti)_{cs}$/A356 RVE model can be divided into three stages, denoted as Stage I, II and III in Fig. 7. Stage I

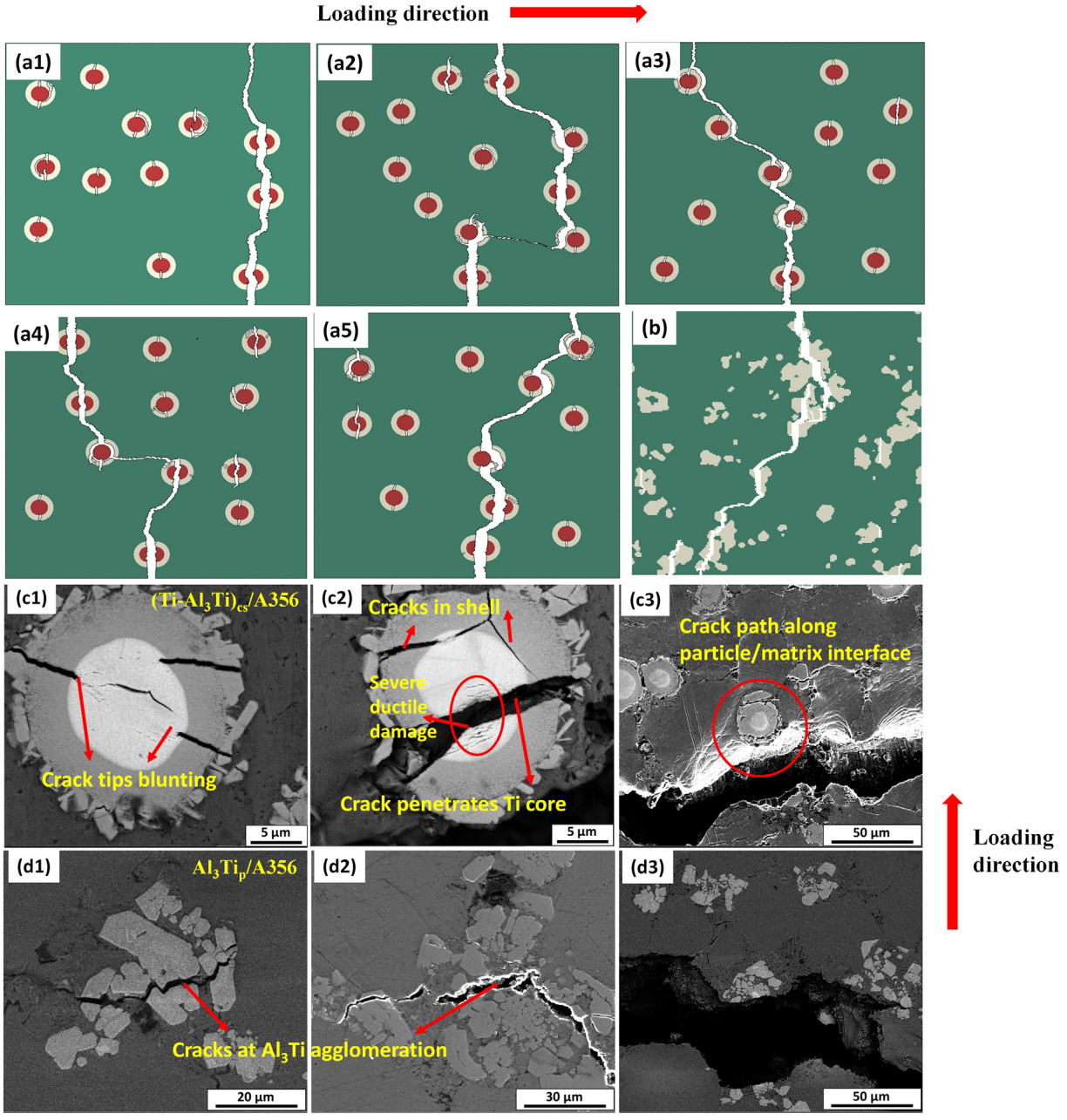

Fig. 9. Simulated crack paths in (a1 to a5) Al_3Ti_p/A356 and (b) $(Ti\text{-}Al_3Ti)_{cs}$/A356 RVE models; (c1 to c3) cracks observed in an Al_3Ti_p/A356 sample and (d1 to d3) in a $(Ti\text{-}Al_3Ti)_{cs}$/A356 sample in in-situ tensile test.

depicts the deformation of RVE before the initiation of cracks (element deletion occurs). In this stage, the stress concentrates on the hard Al_3Ti shell of the particulates. Prior to crack initiation, the true stress on the Al_3Ti shell may exceed 400 MPa. Stage II refers to the particle cracking process, i.e., cracks initiate and grow within the core-shell particulates. From simulation, cracking occurs in the Al_3Ti shell perpendicular to the tensile loading at a nominal strain of 2.2%, as being presented in an enlarged particulate in the second column of Fig. 7(a). As the nominal strain increases to 3%, cracks are shown in all the Al_3Ti shells. After the cracking of an Al_3Ti shell, the ductile Ti core of the core-shell particulate endures a higher stress than the brittle Al_3Ti does, as shown in Fig. 7(b). The true stress taken by the Al_3Ti phase decreases to as low as ~100 MPa, while the true stress of Ti core increases to as much as ~650 MPa. No propagation of cracks in the Al_3Ti shell are observed until the nominal strain reaches 6.1%, when the initial cracks in the Al_3Ti shell extend into the ductile Ti core, within the shell layer or along the Al_3Ti-matrix interface, as seen in the fifth column of Fig. 7 (a). Stage III follows subsequently, referring to the crack propagation and linkage through the A356 matrix until a main crack passes across the entire RVE model, indicating the fracture of the RVE. Throughout Stage III, the stresses taken by all the constitutive phases drop continuously, as presented in the stress-strain curve of A356 matrix in Fig. 7(b).

4.3.2. Al_3Ti_p/A356 composite

Fig. 8(a) shows the Mises Stress distribution, S11 distribution and damage evolution of Al_3Ti_p/A356 RVE model at different nominal strains under tensile loading. Its constitutive true stress-strain relationships of the RVE are presented in Fig. 8(c). Similarly, the deformation of Al_3Ti_p/A356 RVE is divided into two stages. Stage I also presents the deformation of RVE without the occurrence of damage. In this stage, Al_3Ti phase also takes higher stress than the A356 matrix does and the stress concentration is more serious than that in $(Ti\text{-}Al_3Ti)_{cs}$/A356 by comparing the Mises stress distribution in Fig. 8(b). That is attributed to the irregular morphology of the clusters of Al_3Ti particulates compared to the spherical core-shell structured particulates. For the same reason, cracks occur in the Al_3Ti particulates at a lower nominal strain (1.45%) than the required strain in a $(Ti\text{-}Al_3Ti)_{cs}$/A356 RVE (2.2%), as in Fig. 8(a). From Fig. 8(c), the true stress on the Al_3Ti particulates at the end of Stage I is <400 MPa, which is lower than the stress on the Al_3Ti shell in the $(Ti\text{-}Al_3Ti)_{cs}$/A356 composite. Therefore, it is concluded that the irregular shape of monolithic Al_3Ti particulates weakens their strengthening effects.

Stage II follows, starting with the cracking of particulates. The large clusters of Al_3Ti particulates from agglomeration during processing are prone to cracking due to a serious stress concentration as circled in Fig. 8(a). At the nominal strain of 3%, the cracks propagate into the A356 matrix and propagate in the matrix rapidly, resulting in the fracture of RVE at a nominal strain of 3.4%. In Stage II, the stress drops continuously due to a considerable amount of element deletion inside RVE, as mentioned above.

By comparing the constitutive stress partition and damage evolution of the two composites, the combination of higher ductility and strength of $(Ti\text{-}Al_3Ti)_{cs}$/A356 can be attributed to the following two reasons. One is the uniform distribution of spherical reinforcing particulates, which reduce the stress concentration and postpone the damage initiation in brittle Al_3Ti shells, compared to the agglomerated monolithic Al_3Ti particulates. Another significant reason is the blunting of crack tips by both ductile Ti core inside and A356 matrix outside the core-shell particulates, which consumes a large amount of energy and therefore delays the propagation of cracks in the composites effectively. The brittle Al_3Ti shell of a core-shell structured particulate has smooth spherical phase boundaries with the Ti core inside and the A356 matrix outside. It is difficult for the cracks that were initiated in the Al_3Ti shell to extend into the surrounding ductile Ti core and A356 matrix. From Fig. 7(a), despite the occurrence of cracks in the Al_3Ti shell at a rather small nominal strain (2.2%–3%), the cracks do not extend into the A356 matrix under a quite large strain until a nominal strain reaches 6.8%. The ultimate elongation is 8.8% for the model in Fig. 7(a), tripling the elongation of the Al_3Ti_p/A356 composite. Moreover, due to the blunting of crack tips, the Ti core and the A356 matrix are strengthened continuously as presented in Fig. 7(b), which results in the high tensile strength of the $(Ti\text{-}Al_3Ti)_{cs}$/A356 composite.

4.4. Comparison with SEM observation

In-situ tensile test was conducted to observe the fracture of the composites. The results are shown in Fig. 9. Fig. 9(c1–c3) and (d1–d3) were taken during the tensile process to compare with the simulated crack paths of different RVE models in Fig. 9(a1–a5) and (b), respectively.

From both simulation and experimental observation of the Al_3Ti_p/A356 composite, the cracks initiate in the agglomerations of monolithic Al_3Ti particulate, generally perpendicular to the loading direction as shown in Fig. 9(b), (d1) and (d2). Subsequently, the cracks in Al_3Ti particulates are linked through the ductile A356 matrix as seen in Fig. 9(d3) and (b). As to the $(Ti\text{-}Al_3Ti)_{cs}$/A356 composite, the cracks in the Al_3Ti shell are observed along the radial direction and the blunting of crack tips is also substantiated as in Fig. 9(c1), which is in agreement with the radial cracks found in the Al_3Ti shells in the RVE models in Fig. 8 (a). From Fig. 9(c1) and (c2), Ti core suffers a severe ductile damage before cracking, indicating that a high stress is endured by the Ti core. Furthermore, the initial cracks in the Al_3Ti shells can extend into the ductile Ti core, within the shell layer or along the particulate-matrix interface, as seen in Fig. 9(c2) and (c3), which is in accordance with the simulation in five RVE models in Fig. 9(a). In general, from the comparison of simulation and in-situ tensile test results, the 2D simulation results show a satisfactory prediction of the damage evolution microscopically in the two composites. However, 2D simulation still cannot predict the mechanical properties as accurate as 3D simulation does, which is a limitation of the 2D simulation.

5. Conclusion

The mechanical and fracture behaviors of a Ti-Al_3Ti core-shell structured particulate reinforced A356 composite are investigated by microstructure-based FE simulation with 2D RVE models, and compared with the 2D simulation of a monolithic Al_3Ti_p/A356 composite. Uniaxial tensile behavior and microscopic damage evolution in the $(Ti\text{-}Al_3Ti)_{cs}$/A356 composites are simulated in detail to help understand its high ductility and fracture behavior. The following conclusions are summarized: The simulated curves indicate the application of plane stress element underestimates the stress, while applying plane strain element overestimates the stress, compared to the experimental results of the tensile test. With plane stress element and considering the damage evolution, 2D RVE gives a satisfactory prediction of tensile strength and elongation of the $(Ti\text{-}Al_3Ti)_{cs}$/A356 composite.

From the details of microscopic simulation, the high ductility of the $(Ti\text{-}Al_3Ti)_{cs}$/A356 composite is attributed to the uniform distribution of spherical core-shell particulates, which alleviate the stress concentration and postpone the crack initiation in brittle Al_3Ti phase, compared to the agglomerated monolithic Al_3Ti particulates in Al_3Ti_p/A356 composite. Another significant reason is the blunting of crack tips in Al_3Ti shells by the surrounding ductile Ti core and A356 matrix, which delays the crack propagation evidently comparing to the monolithic Al_3Ti_p/A356 composite. After the brittle cracking of Al_3Ti shell, the cracks do not propagate under a nominal strain from 2.2% to 6.1%. Ti core and A356 matrix continue strengthening, meanwhile. Consequently, the $(Ti\text{-}Al_3Ti)_{cs}$/A356 composite shows a significant increase in elongation while reaches a higher tensile strength, compared to the monolithic Al_3Ti_p/A356 composite.

The damage evolution predicted by RVE simulation for both the $(Ti\text{-}Al_3Ti)_{cs}$/A356 and the monolithic Al_3Ti_p/A356 composites show a good agreement to the observation from in-situ tensile test.

CRediT authorship contribution statement

Siming Ma: Writing - original draft, Conceptualization, Methodology. **Xuezheng Zhang:** Validation, Investigation. **Tijun Chen:** Supervision, Investigation, Validation. **Xiaoming Wang:** Supervision, Writing - review & editing.

Declaration of competing interest

The authors declare that they have no known competing financial interests or personal relationships that could have appeared to influence the work reported in this paper.

Acknowledgement

SM acknowledges Purdue University for a Ross Fellowship to support his study with the Purdue Polytechnic Institute. XZ acknowledges Lanzhou University of Technology for the financial support as a visiting scholar to Purdue University.

References

[1] G. Ran, J.E. Zhou, Q.G. Wang, Precipitates and tensile fracture mechanism in a sand cast A356 aluminum alloy, J. Mater. Process. Technol. 207 (2008) 46–52, https://doi.org/10.1016/j.jmatprotec.2007.12.050.
[2] M. Zhu, Z. Jian, G. Yang, Y. Zhou, Effects of T6 heat treatment on the microstructure, tensile properties, and fracture behavior of the modified A356 alloys, Mater. Des. 36 (2012) 243–249, https://doi.org/10.1016/j.matdes.2011.11.018.
[3] Q.G. Wang, C.J. Davidson, Solidification and precipitation behaviour of Al-Si-Mg casting alloys, J. Mater. Sci. 36 (2001) 739–750, https://doi.org/10.1023/A:1004801327556.
[4] S.C. Tjong, Z.Y. Ma, Microstructural and mechanical characteristics of in situ metal matrix composites, Mater. Sci. Eng. R Reports. 29 (2000) 49–113.
[5] Y. Feng, J. Ren, C. Dong, R. Wang, Microstructures and properties of Ti-coated SiC_p reinforced Al-Si alloy composites, JOM 69 (2017) 756–762.
[6] D. Jiang, J. Yu, Simultaneous refinement and modification of the eutectic Si in hypoeutectic Al–Si alloys achieved via the addition of SiC nanoparticles, J. Mater. Res. Technol. 8 (2019) 2930–2943.
[7] S. Tiwari, S. Das, V.A.N. Ch, Mechanical properties of Al–Si–SiC composites, Mater. Res. Express. 6 (2019), 76553.
[8] X. Wang, A. Jha, R. Brydson, In situ fabrication of Al_3Ti particle reinforced aluminium alloy metal–matrix composites, Mater. Sci. Eng. A 364 (2004) 339–345, https://doi.org/10.1016/j.msea.2003.08.049.
[9] Y. Zeng, D. Himmler, P. Randelzhofer, C. Körner, Microstructures and mechanical properties of Al_3Ti/Al composites produced in situ by high shearing technology, Adv. Eng. Mater. (2018) 1800259.
[10] Z. Liu, X. Wang, Q. Han, J. Li, Effects of the addition of Ti powders on the microstructure and mechanical properties of A356 alloy, Powder Technol. 253 (2014) 751–756, https://doi.org/10.1016/j.powtec.2013.12.052.
[11] C. Yang, Z. Liu, Q. Zheng, Y. Cao, X. Dai, L. Sun, J. Zhao, J. Xing, Q. Han, Ultrasound assisted in-situ casting technique for synthesizing small-sized blocky Al_3Ti particles reinforced A356 matrix composites with improved mechanical properties, J. Alloys Compd. 747 (2018) 580–590, https://doi.org/10.1016/j.jallcom.2018.02.010.
[12] Z. Liu, N. Cheng, Q. Zheng, J. Wu, Q. Han, Z. Huang, J. Xing, Y. Li, Y. Gao, Processing and tensile properties of A356 composites containing in situ small-sized Al_3Ti particulates, Mater. Sci. Eng. A 710 (2018) 392–399, https://doi.org/10.1016/j.msea.2017.11.005.
[13] S. Ma, X. Wang, Mechanical properties and fracture of in-situ Al_3Ti particulate reinforced A356 composites, Mater. Sci. Eng. A 754 (2019) 46–56.
[14] Y. Xue, R. Shen, S. Ni, M. Song, D. Xiao, Fabrication, microstructure and mechanical properties of Al–Fe intermetallic particle reinforced Al-based composites, J. Alloys Compd. 618 (2015) 537–544.
[15] T.J. Chen, H. Qin, X.Z. Zhang, Effects of reheating duration on the microstructure and tensile properties of in situ core-shell-structured particle-reinforced A356 composites fabricated via powder thixoforming, J. Mater. Sci. 53 (2018) 2576–2593, https://doi.org/10.1007/s10853-017-1713-2.
[16] W. Wu, B. Guo, Y. Xue, R. Shen, S. Ni, M. Song, Ni-Al_xNi_y core–shell structured particle reinforced Al-based composites fabricated by in-situ powder metallurgy technique, Mater. Chem. Phys. 160 (2015) 352–358.
[17] B. Guo, S. Ni, R. Shen, M. Song, Fabrication of Ti-Al_3Ti core-shell structured particle reinforced Al based composite with promising mechanical properties, Mater. Sci. Eng. A 639 (2015) 269–273, https://doi.org/10.1016/j.msea.2015.05.015.
[18] Y. Wang, M. Song, S. Ni, Y. Xue, In situ formed core-shell structured particle reinforced aluminum matrix composites, Mater. Des. 56 (2014) 405–408, https://doi.org/10.1016/j.matdes.2013.11.030.
[19] T. Chen, L. Geng, H. Qin, M. Gao, Core-shell-structured particle reinforced A356 matrix composite prepared by powder-thixoforming: effect of reheating temperature, Materials (Basel) 11 (2018) 1718.
[20] T. Kanit, S. Forest, I. Galliet, V. Mounoury, D. Jeulin, Determination of the size of the representative volume element for random composites: statistical and numerical approach, Int. J. Solids Struct. 40 (2003) 3647–3679.
[21] A.K. Rana, S.K. Paul, P.P. Dey, Effect of martensite volume fraction on cyclic plastic deformation behavior of dual phase steel: micromechanics simulation study, J. Mater. Res. Technol. 8 (2019) 3705–3712.
[22] B. Anbarlooie, H. Hosseini-Toudeshky, M. Hosseini, J. Kadkhodapour, Experimental and 3D micromechanical analysis of stress–strain behavior and damage initiation in dual-phase steels, J. Mater. Eng. Perform. 28 (2019) 2903–2918.
[23] S. Li, C. Guo, L. Hao, Y. Kang, Y. An, Microstructure-based modeling of mechanical properties and deformation behavior of DP600 dual phase steel, Steel Res. Int. 90 (2019) 1900311.
[24] M.A. Eltaher, A. Wagih, Micromechanical modeling of damage in elasto-plastic nanocomposites using unit cell representative volume element and cohesive zone model, Ceram. Int. (2020)(In press, corrected proof.).
[25] L. Weng, T. Fan, M. Wen, Y. Shen, Three-dimensional multi-particle FE model and effects of interface damage, particle size and morphology on tensile behavior of particle reinforced composites, Compos. Struct. 209 (2019) 590–605.
[26] B. Nayak, R.K. Sahu, Experimental and Digimat-FE based representative volume element analysis of exceptional graphene flakes/aluminium alloy nanocomposite characteristics, Mater. Res. Express. 6 (2019), 116593.
[27] J.F. Zhang, H. Andrae, X.X. Zhang, Q.Z. Wang, B.L. Xiao, Z.Y. Ma, An enhanced finite element model considering multi strengthening and damage mechanisms in particle reinforced metal matrix composites, Compos. Struct. 226 (2019) 111281.
[28] L. Arnberg, L. Backerud, H. Klang, Grain refinement of aluminium 2: intermetallic particles in master alloys for grain refinement of aluminium, Met. Technol. 1693 (1982) 7–13, https://doi.org/10.1179/030716982803286368.
[29] Z. Liu, Q. Han, J. Li, Fabrication of in situ Al_3Ti/Al composites by using ultrasound assisted direct reaction between solid Ti powders and liquid Al, Powder Technol. 247 (2013) 55–59, https://doi.org/10.1016/j.powtec.2013.07.005.
[30] S. Ghosh, S. Moorthy, Particle fracture simulation in non-uniform microstructures of metal-matrix composites, Acta Mater. 46 (1998) 965–982, https://doi.org/10.1016/S1359-6454(97)00289-9.
[31] M. Dao, N. Chollacoop, K.J. Van Vliet, T.A. Venkatesh, S. Suresh, Computational modeling of the forward and reverse problems in instrumented sharp indentation, Acta Mater. 49 (2001) 3899–3918, https://doi.org/10.1016/S1359-6454(01)00295-6.
[32] A.C. Fischer-Cripps, Nanoindentation, 2011https://doi.org/10.1007/978-1-4419-9872-9.
[33] C. Leyens, M. Peters, Edited by Handbook of Cellular Metals Phase Transformations in Materials, 2003.
[34] C.L. Fu, Electronic, elastic, and fracture properties of trialuminide alloys: Al_3Sc and Al_3Ti, J. Mater. Res. 5 (1990) 971–979, https://doi.org/10.1557/JMR.1990.0971.
[35] R.B. King, Elastic analysis of some punch problems for a layered medium, Int. J. Solids Struct. 23 (1987) 1657–1664.
[36] U. Bathini, T.S. Srivatsan, A. Patnaik, T. Quick, A study of the tensile deformation and fracture behavior of commercially pure titanium and titanium alloy: influence of orientation and microstructure, J. Mater. Eng. Perform. 19 (2010) 1172–1182, https://doi.org/10.1007/s11665-010-9613-5.
[37] J.R. Rice, D.M. Tracey, On the ductile enlargement of voids in triaxial stress fields, J. Mech. Phys. Solids. 17 (1969) 201–217.
[38] H. Qing, 2D micromechanical analysis of SiC/Al metal matrix composites under tensile, shear and combined tensile/shear loads, Mater. Des. 51 (2013) 438–447, https://doi.org/10.1016/j.matdes.2013.04.051.
[39] N. Srinivasan, R. Velmurugan, R. Kumar, S.K. Singh, B. Pant, Deformation behavior of commercially pure (CP) titanium under equi-biaxial tension, Mater. Sci. Eng. A 674 (2016) 540–551, https://doi.org/10.1016/j.msea.2016.08.018.
[40] Z. Lu, N. Wei, P. Li, C. Guo, F. Jiang, Microstructure and mechanical properties of intermetallic Al_3Ti alloy with residual aluminum, Mater. Des. 110 (2016) 466–474, https://doi.org/10.1016/j.matdes.2016.08.025.
[41] H. Qing, Automatic generation of 2D micromechanical finite element model of silicon-carbide/aluminum metal matrix composites: effects of the boundary conditions, Mater. Des. 44 (2013) 446–453, https://doi.org/10.1016/j.matdes.2012.08.011.
[42] X. Zhuang, S. Ma, Z. Zhao, Effect of particle size, fraction and carbide banding on deformation and damage behavior of ferrite-cementite steel under tensile/shear loads, Model. Simul. Mater. Sci. Eng. 25 (2017) 1–30, https://doi.org/10.1088/1361-651X/25/1/015007.
[43] J. Zhou, A.M. Gokhale, A. Gurumurthy, S.P. Bhat, Realistic microstructural RVE-based simulations of stress-strain behavior of a dual-phase steel having high martensite volume fraction, Mater. Sci. Eng. A 630 (2015) 107–115, https://doi.org/10.1016/j.msea.2015.02.017.
[44] X. Sun, K.S. Choi, W.N. Liu, M.A. Khaleel, Predicting failure modes and ductility of dual phase steels using plastic strain localization, Int. J. Plast. 25 (2009) 1888–1909, https://doi.org/10.1016/j.ijplas.2008.12.012.
[45] A. Ramazani, K. Mukherjee, A. Schwedt, P. Goravanchi, U. Prahl, W. Bleck, Quantification of the effect of transformation-induced geometrically necessary dislocations on the flow-curve modelling of dual-phase steels, Int. J. Plast. 43 (2013) 128–152, https://doi.org/10.1016/j.ijplas.2012.11.003.
[46] M.M. Aghdam, S.R. Morsali, Damage initiation and collapse behavior of unidirectional metal matrix composites at elevated temperatures, Comput. Mater. Sci. 79 (2013) 402–407, https://doi.org/10.1016/j.commatsci.2013.06.024.
[47] N.K. Sharma, R.K. Misra, S. Sharma, Finite element modeling of effective thermomechanical properties of Al–B_4C metal matrix composites, J. Mater. Sci. 52 (2017) 1416–1431, https://doi.org/10.1007/s10853-016-0435-1.

[48] R. Kapoor, N. Kumar, R.S. Mishra, C.S. Huskamp, K.K. Sankaran, Influence of fraction of high angle boundaries on the mechanical behavior of an ultrafine grained Al–Mg alloy, Mater. Sci. Eng. A 527 (2010) 5246–5254.
[49] S.K. Paul, Micromechanics based modeling of Dual Phase steels: prediction of ductility and failure modes, Comput. Mater. Sci. 56 (2012) 34–42, https://doi.org/10.1016/j.commatsci.2011.12.031.
[50] G. Tursun, U. Weber, E. Soppa, S. Schmauder, The influence of transition phases on the damage behaviour of an Al/10vol.%SiC composite, Comput. Mater. Sci. 37 (2006) 119–133, https://doi.org/10.1016/j.commatsci.2005.12.018.
[51] Q.G. Wang, Microstructural effects on the tensile and fracture behavior of aluminum casting alloys A356/357, Metall. Mater. Trans. A. 34 (2003) 2887–2899, https://doi.org/10.1007/s11661-003-0189-7.